Superconductor Science and Technology

A 6-around-1 cable using high-temperature superconducting STAR® wires for magnet applications

To cite this article before publication: Nathaly Castaneda *et al* 2024 *Supercond. Sci. Technol.* in press https://doi.org/10.1088/1361-6668/ad20fb

A 6-around-1 cable using high-temperature superconducting STAR® wires for magnet applications

Nathaly Castaneda[1], Paolo Ferracin[2], Cyrus Funkhouser[3], Eduard Galstyan[3], Hugh C. Higley[2], Sri Ram Korupolu[4], Goran Majkic[4], Hoang Nguyen[3], Soren O. Prestemon[2], Venkat Selvamanickam[4], Huy Truong[4], Xiaorong Wang[2]

[1] Mechanical Engineering Technology and Materials Science and Engineering, University of Houston, Houston, TX 77204, USA

[2] Lawrence Berkeley National Laboratory, Berkeley, CA 94720, USA

[3] AMPeers LLC, Houston, TX 77059, USA

[4] Department of Mechanical Engineering, Advanced Manufacturing Institute, Texas Center for Superconductivity, University of Houston Houston, TX 77024, USA

E-mail: vselvama@central.uh.edu, xrwang@lbl.gov

Abstract. To generate a dipole field above 20 T, we need high-temperature superconductors, including $REBa_2Cu_3O_{7-x}$ (RE = rare earth, REBCO) coated conductors. However, the optimal architecture of a high-current flexible REBCO cable is not yet settled for high-field magnet applications. Here we report a 6-around-1 cable concept based on the high-temperature superconducting STAR® wires. We made two cable samples. One had a single STAR® wire and the other had six STAR® wires. The cable with six STAR® wires was 1.5 m long. It had a diameter of 5.7 mm and a pitch length of 52 mm. The critical current of the cable before bending was 1448 A at 77 K, retaining at least 77% of the total critical current from individual STAR® wires. The cable had a low n value around 4.5. At a bend radius of 30 mm, the critical current and n value remained the same as before bending. The total resistance of electrical terminations was 61 nΩ at 77 K. The flexible and transposed 6-around-1 STAR® cable can provide another route toward practical REBCO conductors for high-field accelerator and fusion magnet applications.

1. Introduction

Accelerator magnets with a dipole field of 20 T for future circular colliders need high-temperature superconductors, such as $Bi_2Sr_2CaCu_2O_x$ (Bi-2212) round wires and $REBa_2Ca_3O_{7-x}$ (REBCO, RE = rare earth) coated conductors [1, 2]. In collaboration with industry partners, the U.S. Magnet Development Program (MDP) is developing magnet technology for both conductors [3–11].

Two REBCO conductors, CORC® and STAR® wires, are being studied within the MDP. Both conductors are made by wrapping multiple REBCO tapes around a round core, resulting in a macroscopic round wire [12–15]. The REBCO tapes are twisted but not transposed in either conductor architecture [16].

Leveraging the unique REBCO tape where the superconducting film is positioned at the neutral plane, STAR® wires have a typical diameter of 1.5 – 3 mm and a minimum bend radius of 15 mm [14, 15]. Both features can facilitate a cable consisting of multiple STAR® wires.

A high-current multi-wire cable can reduce magnet inductance, important for the quench protection of high-field magnets storing a significant amount of energy. Therefore, we explore concepts for a high-current and flexible cable using multiple STAR® wires. One example is a ribbon cable using two wires [17]. The wires, however, are not transposed in a ribbon cable.

Synchrotron accelerator magnets and central solenoid magnets in a tokamak operate with alternating currents. These magnets require transposed cables [18, 19]. Rutherford cable, ubiquitous in superconducting accelerator magnets since the Tevatron, is a classic example of a transposed cable [18, 20]. Rutherford-type cable using stacked REBCO tapes have also been successfully demonstrated [21–24].

Another transposed configuration is a 6-around-1 cable. Each of the six wires wraps around a central wire. Although this configuration has a lower filling factor than a Rutherford cable, it allows a more gentle bend of the wire, attractive for strain-sensitive conductors. Various conductors have been made into 6-around-1 cables [25–30].

Although the idea of a 6-around-1 cable using STAR® wires is intuitive, limited experimental data are available for such a cable. Also, compact 6-around-1 cables with high whole-conductor current density and good bend properties, both needed for high-field accelerator magnets, have not been demonstrated using REBCO conductors. To test the idea, we made two 6-around-1 cable samples using STAR® wires. Here we report the details of the cables, electrical terminations, test results and future steps.

The cables had a diameter around 5 — 6 mm and a twist pitch length of 52 mm. Both cables retained 77%—80% of the total critical current of individual STAR® wires at 77 K. The cables were wound to successively smaller radii and showed less than 5% degradation in critical current at 30 mm bend radius.

Our results demonstrated a first step toward a compact 6-around-1 cable using STAR® wires, setting a stage for further development toward a high-current, flexible and transposed conductor for high-field magnet applications.

2. STAR® wires and 6-around-1 cable

AMPeers provided seven STAR® wires. Each STAR® wire had several REBCO tapes wrapped around a core, one tape in a layer. The tape width increased from 1.6 mm in the inner layers to 2.5 mm in the outer layers. The core was a bare Nb-Ti wire with a diameter of 0.7 mm. The wires had no electrical insulation. Table 1 lists the main properties of each wire. Wire 0 was 1 m long and the others were 2 m long.

Table 1. Properties of the STAR® wires used in two 6-around-1 cables. AMPeers measured the critical current at 77 K, self-field before cabling. The critical current and n value were determined at a voltage criterion of 20 μV.

Wire	Diameter mm	Tape count	I_c A	n value
0	1.84	9	495	40
1	1.84	9	340	8
2	1.82	9	335	15
3	1.76	7	$\sim$ 129	9
4	1.74	7	309	21
5	1.71	7	358	43
6	1.92	7	387	37

Wire 3 originally had 9 tapes and a critical current, I_c, of 229 A. We broke the two outermost tapes during cabling. The resulting I_c was estimated to be around 129 A at 77 K, self-field, based on the I_c of the individual tapes measured before fabricating Wire 3.

We made two samples, Cables 1c and 6a. Figure 1 shows the arrangement of the STAR® wire in each cable.

Cable 1c was made in January 2022 using Wire 0 and six 1.63 mm diameter bare Cu wires. The cable had a nominal diameter of 5.2 mm and was 0.6 m long between the electrical terminations.

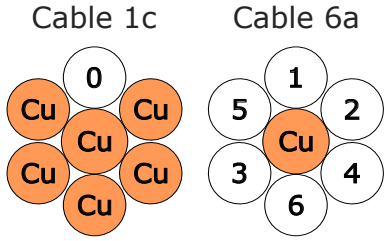

Figure 1. Arrangement of the STAR® wires in two 6-around-1 cables. The numbers represent the wires in table 1.

Cable 6a was made in March 2022 using Wires 1 – 6 and a 2.55 mm diameter bare Cu wire. We arranged the wires according to their nominal diameters. The cable had a nominal diameter of 5.7 mm and was 1.5 m long between the electrical terminations. Figure 2 shows a segment of Cable 6a.

Figure 2. Cable 6a had a nominal diameter of 5.7 mm and a twist pitch length of 52 mm. Each STAR® wire is also labeled.

Both cables were made using a bench-top cabling machine at Lawrence Berkeley National Laboratory (figure 3). The STAR® wires, each mounted on a 100 mm diameter supply spool, were cabled around the central Cu wire under a tension of about 10 N per wire. Torsion control for all of the supply spools was provided through adjustable geared planetary motion. Cabling pitch length was controlled by adjustable gearing. Both cables had a nominal twist pitch length of 52 mm.

Figure 3. Hugh Higley and the cabling machine. A youtube video shows the cabling process.

3. Flute-type electrical termination

The electrical termination for the 6-around-1 cable shared the basic concept and fabrication procedure for a single STAR® wire [17].

We first wrapped an indium wire around the cable for several turns for two purposes (figure 4(a)). First, to mark the end position of the termination. Second, to prevent the cable from being disassembled when we unwound the STAR® wires to trim the REBCO tapes [31]. We constrained the exposed tapes with a fine Cu wire (figure 4(b)). The tape end was soldered with minimum indium to the tape below.

The next step was to install the voltage-tap instrumentation wires. Section 4 has details on the location of voltage taps inside the termination. The insulated instrumentation wire had a diameter of 0.2 mm.

For Cable 1c, we wrapped the instrumentation wire around Wire 0 for two turns and then soldered the tip of the instrumentation wire to the nearby REBCO tape with indium. We then put the processed wire end back into the original cable form.

For Cable 6a, the processed wire ends were first bundled back into the original cable form. We wrapped around the cable end with the fine Cu wire to ensure the bundle can fit inside a

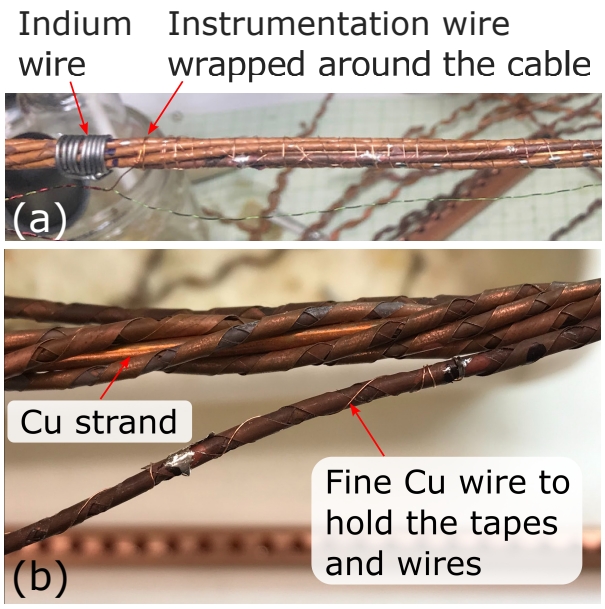

Figure 4. (a) Instrumentation wire was wrapped around a cable sample for two turns. An indium wire wrapped around the cable is also visible. (b) The processed end of the STAR® wire.

Cu termination tubing. The instrumentation wire, with the insulation removed, was then wrapped around the cable for two turns at specific locations, electrically in contact with all six STAR® wires (figure 4(b)).

Finally, we removed the indium wire and inserted the cable end together with the instrumentation wires into the Cu termination tubing. The tubing was 200 mm long with an inner diameter of 6.31 mm and an outer diameter of 7.94 mm. An array of holes was drilled along the tubing for indium filling.

After sealing both ends of the Cu tubing with a aluminum foil, we clamped the Cu tubing horizontally into a heater block (figure 5(a)). Indium strips covered the top of the Cu tubing before the heater was turned on. Once the temperature of the tubing reached around 156°C, the indium strips melted and started filling the Cu tubing through the holes. The heater was on for about 11 minutes. Then we turned it off, cooled down the termination and removed the excessive indium solder from the Cu tubing.

Figure 5(b) shows a finished termination. We called it a flute-type termination because the Cu tubing resembled a bamboo flute.

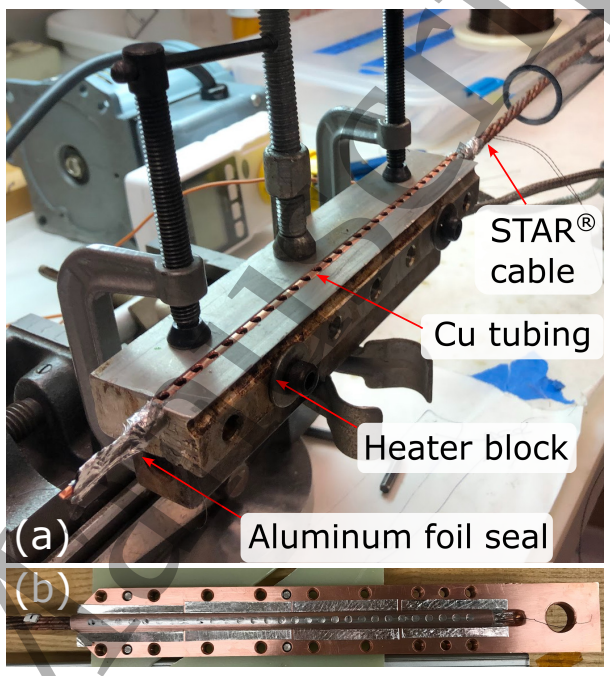

Figure 5. (a) Setup to fill the flute-type termination with indium solder. (b) Finished termination placed in a Cu block.

4. Instrumentation and measurement protocol

To measure the voltage across the cable as a function of current, we installed three voltage taps in each termination (figure 6). The first tap ended within 10 mm of the near end of the Cu tubing. The second tap was placed in the center of the Cu tubing. The third one was outside the Cu tubing, connecting to the central Cu strand of the cable.

For Cable 1c, although the tips of the first two instrumentation wires were soldered to nearby tapes, they may detach from the tape but remain embedded in the solder when

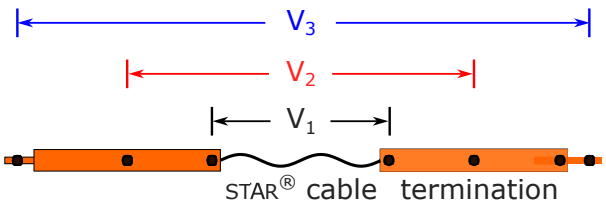

Figure 6. Locations of the voltage taps inside the terminations, denoted by the solid black circles. The voltage signal generated from each pair of taps is also shown.

we filled the Cu tubing with indium solder. For Cable 6a, the instrumentation wire was electrically in contact with all six STAR® wires.

Outside the terminations, the instrumentation wires followed the STAR® wires to minimize the inductive pickup.

All the electrical measurements were performed with the sample submerged in liquid nitrogen at 77 K. The critical current and n value of the cable were determined, by fitting the measured $V(I)$ data from the inner most pair of voltage taps, according to a power law [32]

$$V = V_{\mathrm{o}} + IR_{\mathrm{t}} + V_{\mathrm{c}}\left(\frac{I}{I_{\mathrm{c}}}\right)^{n}, \qquad (1)$$

where V_{o} is the voltage offset, R_{t} is the termination resistance, and V_{c} is the voltage criterion. The I_{c} and n value were determined at a voltage criterion of 20 μV, corresponding to an electric-field criterion of 33 μV m^{-1} for Cable 1c and 13 μV m^{-1} for Cable 6a.

We first measured the critical current of Cable 1c in a background field at 77 K before bending. The cable was sandwiched in the gap between a split pair of Cu solenoid coils. The magnetic field was transverse to the longitudinal axis of Cable 1c. About 50 mm long of Cable 1c was covered by the uniform applied field.

We used a set of fixtures to measure the critical current of the cable at different bend radii. G10 boards with a circular side were used for the bend radius of 200 and 100 mm. For smaller bend radii, we used fixtures that had several turns of groove. The groove had a nominal diameter of 6.2 mm. The central axis of the groove followed a circular helix with a nominal pitch length of 7.2 mm. We printed five fixtures using Accura® Bluestone®, covering a radius of 75, 60, 45, 30 and 20 mm for the circular helix. We used the radius of the circular helix as the bend radius of the cable because of the relatively small pitch length of the circular helix.

Pulling both terminations away from the bending fixture, we bent the sample for half a turn around the fixture when the bend radius was less than 100 mm, leading to a hair-pin bend. At least one twist pitch length of the cable was bent around each radius. At 20 mm radius, Cable 1c was also wound for 1.5 turns around the fixture. Figure 7 shows Cable 1c was bent to 200 and 20 mm radius.

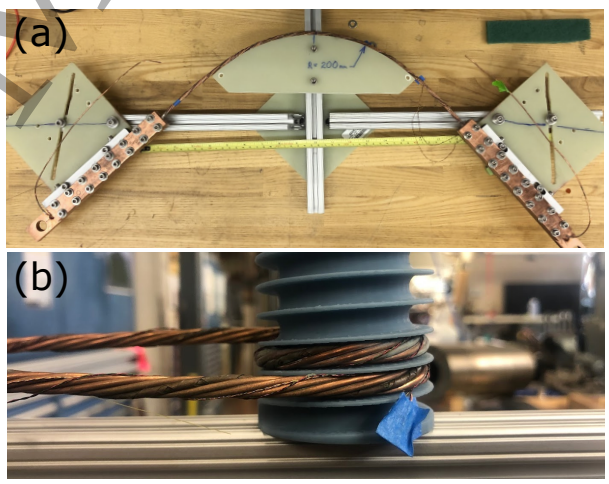

Figure 7. Cable 1c was bent to (a) 200 mm radius and (b) 1.5 turns at 20 mm radius.

For Cable 6a, we measured its critical current before bending. Then we wound it into a canted $\cos\theta$ (CCT) coil configuration and measured the critical current again (figure 8(a)). The minimum bend radius of the cable was 75 mm in the CCT configuration.

We unwound the cable from the CCT former and bent it into successively smaller radii (figure 8(b)).

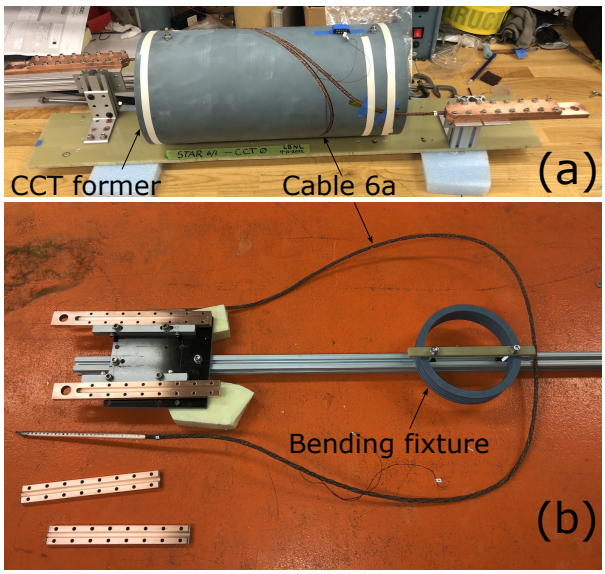

Figure 8. (a) Cable 6a was wound into a CCT coil configuration. (b) Cable 6a was unwound from the coil former for the bending test at 75 mm radius.

After the hair-pin bend at the final 30 mm radius, we wound Cable 6a around the bending fixture for 6.5 turns, resulting in a small solenoid coil (figure 9). We inserted a calibrated cryogenic Hall sensor (Lake Shore HGCA 3020) at the center of the aperture of the fixture to measure the solenoid field of the coiled Cable 6a. We also measured the $V(I)$ transition and solenoid field with the current ramping at different rates.

Both cable samples went through several thermal cycles. We bent the cable samples at room temperature, cooled them down to 77 K and measured the critical current, and then warmed them up to room temperature for the next smaller bend radius.

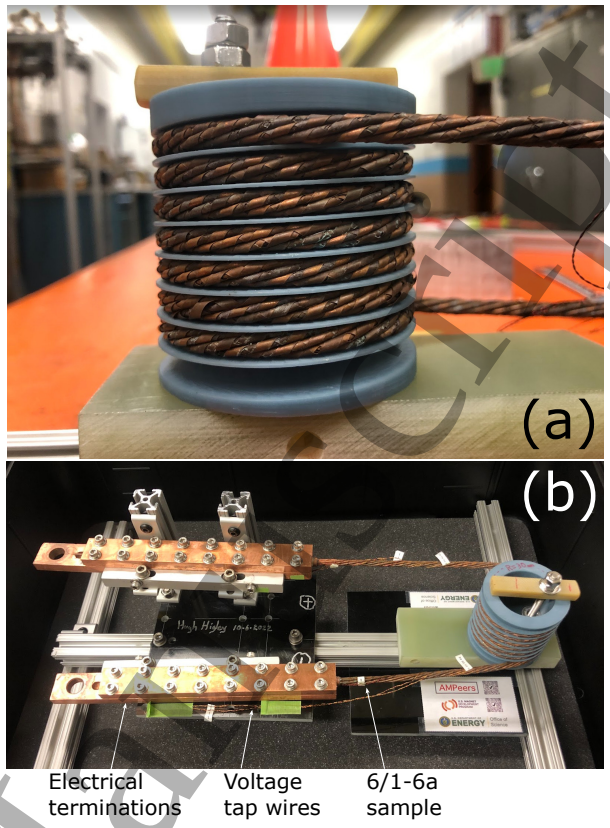

Figure 9. (a) Cable 6a was wound for 6.5 turns at a radius of 30 mm. (b) The measurement setup.

5. Measurement results of Cable 1c

5.1. Critical current as a function of applied transverse field

Figure 10 shows that the critical current of Cable 1c decreased with the applied magntetic field at 77 K. The critical current reduced by 50% from self-field to an applied flux density of 540 mT.

The n value generally decreased with the applied magnetic field (figure 11).

Figure 12 shows the $V_1(I)$ curves measured at self-field, an applied flux density of 273 mT and 546 mT. At self-field, a slow but visible voltage rise started around 150 A, followed by a sharper rise when the voltage was above 10 μV. The $V(I)$ curve deviated from the power-law fit due to the early voltage rise.

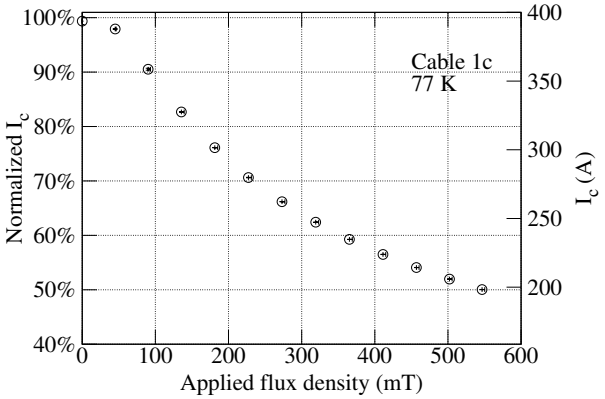

Figure 10. The critical current of Cable 1c as a function of the applied flux density transverse to the cable axis. 77 K. Primary y axis: critical current normalized to the self-field value. Secondary y axis: actual I_c values. The x error bars represent the uncertainty of the measured applied flux density. The measurement error of the critical current was ±0.5%.

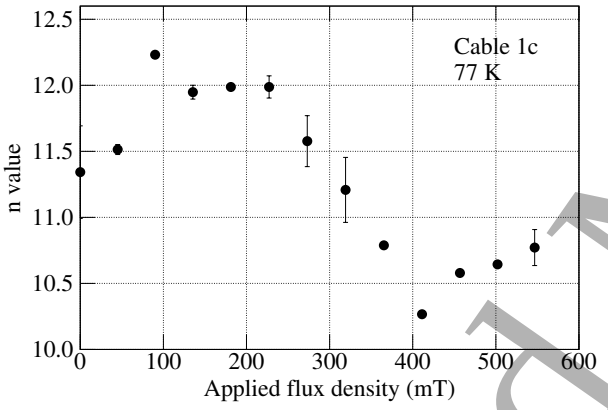

Figure 11. The n value of Cable 1c as a function of the applied flux density transverse to the cable axis. 77 K. The y error bars represent the range of the measured n values.

The deviation, however, became less as the applied field increased.

5.2. Critical current as a function of bend radius

Figure 13 shows the $V(I)$ curves of Cable 1c at different bend radii. The voltage was measured when the current was held constant. The critical current of the straight cable was 398 A with an n value of 12. The $V(I)$ data of

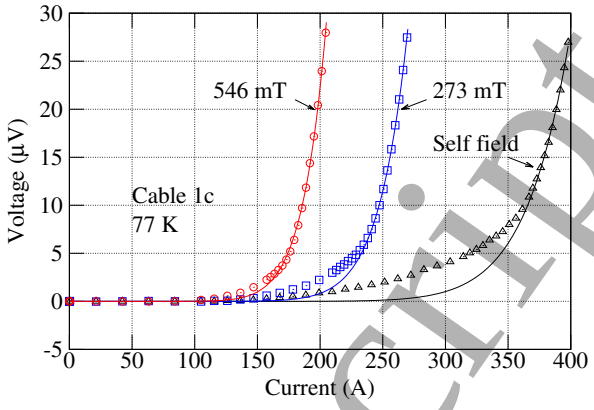

Figure 12. The $V_1(I)$ behavior of Cable 1c in different background fields. 77 K. Symbols: measurement. Lines: fit to the voltage data above 10 μV using (1).

Wire 0 measured before cabling by AMPeers were also shown.

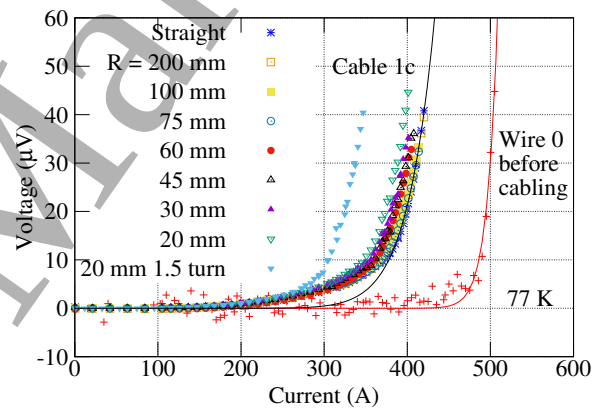

Figure 13. Voltage V_1 across Cable 1c as a function of current and bend radius. 77 K, self-field. Measured data are in symbols. Solid lines are fit to the voltage data above 10 μV using (1).

At a bend radius of 20 mm, the critical current decreased by 6.3% from that of the straight cable (figure 14). Figure 15 shows the resulting n value as a function of bend radius.

5.3. Termination performance

The measured $V(I)$ curves started with a linear portion at low current. We used the slope of the linear portion as the total

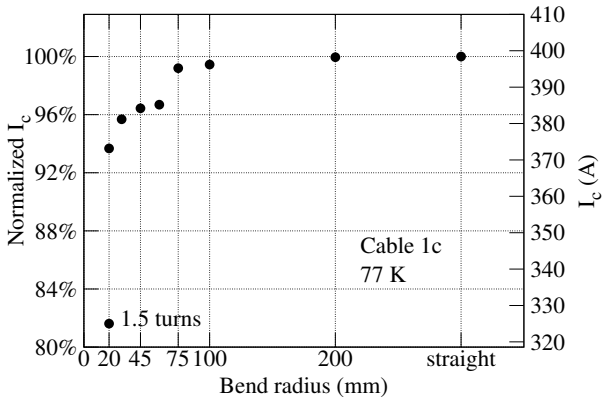

Figure 14. The critical current of Cable 1c as a function of bend radius. 77 K, self-field. The primary y axis gives the values normalized to that measured before bending. The secondary y axis gives the actual values. The measurement error of the critical current was ±0.5%.

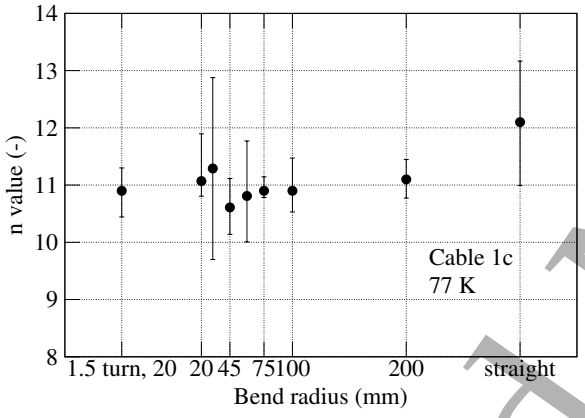

Figure 15. The n value of Cable 1c as a function of bend radius. 77 K, self-field. The error bars represent the range of the measured n value.

resistance of both terminations. Table 3 lists the resistances when Cable 1c was straight and after it was wound around 20 mm radius for 1.5 turns. $R_{t,1}$ was determined from $V_1(I)$, $R_{t,2}$ from $V_2(I)$ and $R_{t,3}$ from $V_3(I)$ (figure 6).

We used computed tomography (CT) scans to evaluate the solder distribution inside a flute-type termination [33]. Figure 16 shows two micro-CT scan images of a 30 mm long segment of a prototype termination. The termination was made for a test sample that

Table 2. The total resistance of both terminations, in nΩ, from three locations of the terminations. Cable 1c. 77 K, self-field.

	Straight	20 mm bend radius
$R_{t,1}$	24.8	23.6
$R_{t,2}$	49.8	47.1
$R_{t,3}$	453	495

had a single STAR® wire and six Cu strands, similar to Cable 1c. The termination had the identical dimensions to those reported here.

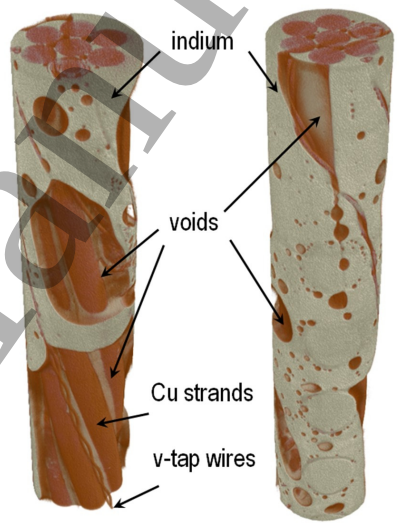

Figure 16. Micro-CT images of a segment of a prototype termination, viewed from two directions. The outer Cu tubing is not shown.

Although the solder filled one side of the termination (figure 16 right), two large voids appeared on the other side, exposing the transposed wires (figure 16 left). The solder filled small gaps between the wires.

6. Measurement results of Cable 6a

6.1. Critical current as a function of bend radius

Figure 17 shows the voltage V_1 across Cable 6a as a function of current and bend radius.

The voltage was measured when the current was held constant.

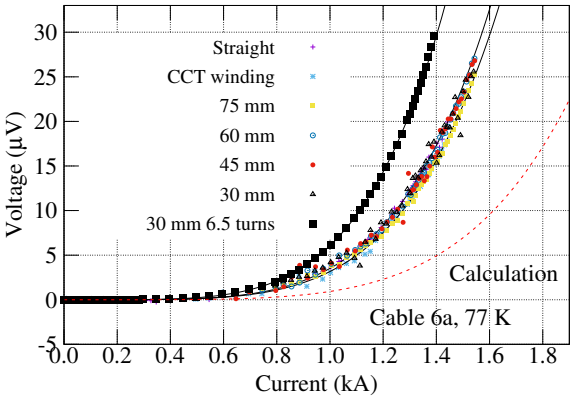

Figure 17. Voltage V_1 across Cable 6a as a function of current and bend radius. 77 K, self-field. Measured data are in symbols. Solid lines are fit using (1). The dashed line is the calculated $V(I)$ curve based on the critical current of individual strand and an n value of 4.5.

The critical current of Cable 6a was 1448 A before bending at 77 K, self-field. Figure 18 shows the evolution of the critical current at different bend radii. Figure 19 shows the measured n value.

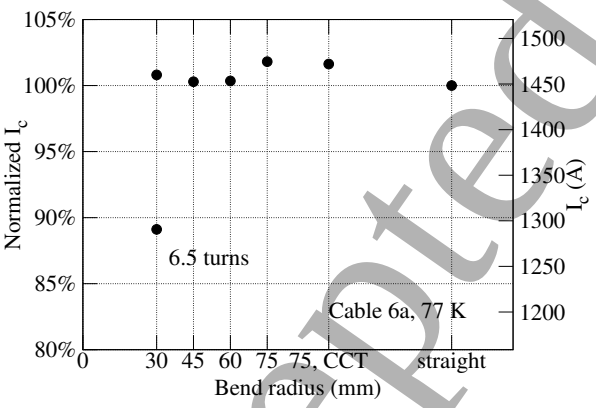

Figure 18. The critical current of Cable 6a as a function of bend radius. 77 K, self-field. The primary y axis gives the values normalized to the I_c measured before bending. The secondary y axis gives the actual values. The measurement error of the critical current was ±0.5%.

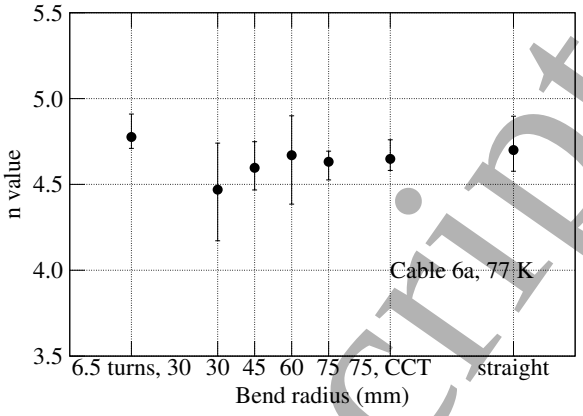

Figure 19. The n value of Cable 6a as a function of bend radius. 77 K, self-field. The error bars represent the range of the measured n value.

6.2. Ramp-rate dependence

Figure 20 shows the $V_1(I)$ curves of the coiled Cable 6a at different ramp rates of the current. The average speed of the current ramp between 0 and the plateau of 1390 A was reported as the ramp rate. The dc data were from figure 17.

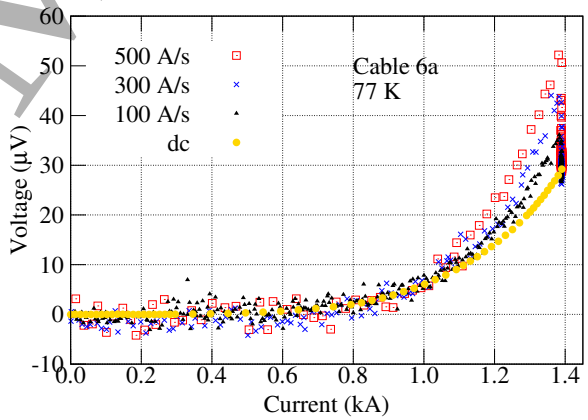

Figure 20. Voltage V_1 across Cable 6a as a function of current and its ramp rate. 6.5 turns at 30 mm radius. 77 K, self-field.

At the same current above 1 kA, the voltage across the cable increased with a higher ramp rate. When the current reached the plateau, the voltage started decaying to the same level as measured at the dc condition at 1390 A, independent of the ramp rate.

A similar ramp-rate dependence was also observed at larger bend radii.

Figure 21 shows the transfer function of the solenoid field at different ramp rates. The transfer function is the ratio between the measured flux density and the measured cable current. The Hall-probe voltage data at the end of the cooldown from room temperature to 77 K was removed as the offset. The measured transfer function was 2% higher than the calculated value.

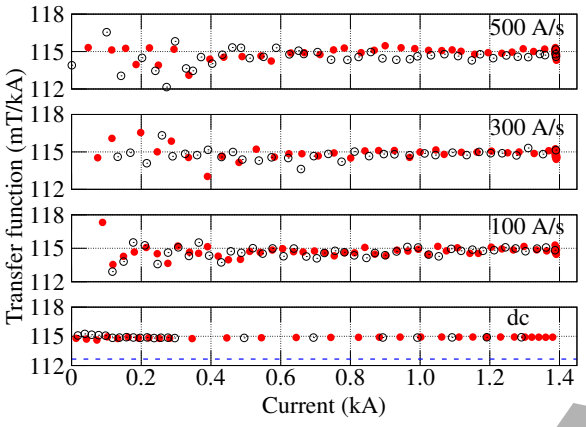

Figure 21. The transfer function of the center solenoid field. 77 K, self-field. Red solid circles: data measured during the up ramp of the current; black open circles: data measured during the down ramp. The dashed line is the calculated value.

6.3. Termination performance

Table 3 lists the total resistances of both terminations when the cable was straight and after it was wound around 30 mm radius for 6.5 turns.

7. Discussion

7.1. I_c retention after cabling

Cable 1c, containing STAR® Wire 0, retained 80% of the critical current of Wire 0 measured before cabling. Cable 6a, containing STAR® Wires 1—6, retained 77% of the total critical current of individual wires (table 1). The actual retention for Cable 6a was likely 2% to 3% higher due to the higher self fields on the wires after cabling and the field dependence of the wire I_c (figure 10 and table A2).

Table 3. The total resistance of both terminations, in nΩ, from three locations of the terminations. Cable 6a. 77 K, self-field.

	Straight	30 mm bend radius
$R_{t,1}$	2.7	1.0
$R_{t,2}$	7.8	5.9
$R_{t,3}$	46.7	61.2

Why the critical current decreased after cabling remains to be clarified. Although the self-field on the STAR® wire increased after cabling for both cables, it was insufficient to cause a 20% I_c reduction in either cable sample (figure 10).

We also do not expect the bending strain to degrade the wires during cabling. The bend radius along the wire axis was about 38 mm based on the wire diameter and cable pitch length, more than twice of the 15 mm minimum bend radius for STAR® wires [34, 35].

On the other hand, the cabling process continuously bent the STAR® wire along its entire length and the gaps between the tapes (figures 4(b) and 9(a)) may strain and degrade the tapes that were sliding against each other during the bending, leading to multiple local degradation during the cabling process.

The early voltage rise itself in Cable 1c does not necessarily mean that Wire 0 degraded. The wire had REBCO tapes of different widths and critical currents [33, 34]. Due to the non-uniform critical current among the REBCO tapes, one tape can reach its critical current before other tapes, leading to an early

voltage rise across the wire and a deviation from the power-law relationship between the voltage and sample current [36, 37]. An early voltage rise can be intrinsic to a STAR® wire containing REBCO tapes of different I_c.

That Wire 0 did not show an early voltage rise before cabling (figure 13) was likely because the voltage taps were attached to the outermost REBCO tape outside the terminations. This approach can yield a $V(I)$ behavior resembling that of a single tape such as a zero resistive slope and a relatively high n value. The $V(I)$ data measured before cabling may not necessarily represent the behavior of a STAR® wire containing multiple tapes.

The applied magnetic field can suppress the early voltage rise (figure 12). The applied field, perpendicular to the broad surface of the REBCO tapes, reduced the tape critical current at 77 K, starting from the outer-layer wider tapes that had a higher critical current. The critical current of the tapes therefore became more uniform and hence less early voltage rise.

To clarify if cabling with continuous bending at a specific radius degraded the wires, we may vary the cable twist pitch length and compare the resulting I_c retention. To have a direct comparison, the locations of the voltage taps should be identical before and after cabling. The cable can have a single STAR® wire to minimize the impact of self-field.

Contrary to Cable 1c, Cable 6a showed a low n value of 4.5 without a pronounced early voltage rise (figure 17). One explanation could be that the n value of the wires were uniformly low around 4.5. As discussed earlier, the n values in table 1 are likely higher than those of the actual wires. We also cannot rule out the wire degradation during the cabling process that can reduce the n value of the cable.

7.2. Cable performance

Both cables were resilient to bending. At a bend radius of 20 mm, the critical current of Cable 1c decreased by 6.3% from that before bending (figure 14). The critical current of Cable 6a at 30 mm bend radius remained the same as before bending (figure 18). A bend radius of 20 — 30 mm is useful to make magnets that require tight bend of conductors.

We attributed the I_c decrease in Cable 1c to the degradation of outer-layer tapes in the STAR® wire. For the $V(I)$ curves in figure 13, we may define two current levels associated with the voltage rise. First, the sharp-rise level at which the sharp voltage rise started above 10 μV. The sharp-rise current level was determined by the outer-layer tapes that had a higher critical current. Second, the early-rise level at which the wire voltage started rising. The early-rise current level was determined by the inner-layer tapes that had the lowest critical current. As the bend radius decreased, the sharp-rise level decreased while the early-rise level remained the same (figure 13), indicating that the outer-layer tapes degraded during bending.

The critical current of Cable 6a reduced by 10% only after the cable was wound for 6.5 turns at 30 mm bend radius. We attributed the reduction to the higher field on the wire in the 6.5-turn coil. It was about 100 mT transverse to each wire carrying 140 A (table A2). The increased field was sufficient to reduce the wire I_c by 10% (figure 10). However, we cannot rule out that when winding the small solenoid at 30 mm radius, the potential mechanical damage to the REBCO tapes, especially the outermost one in the STAR® wires, can cause the observed I_c degradation.

Both cables survived multiple cooldown and warmup thermal cycles between room

temperature and 77 K.

The electrical termination yielded acceptable performance. The total resistance of both terminations of Cable 6a was 61 nΩ at 77 K, lower than that of a previous concept for STAR® wires [17]. We expect the total resistance to be lower than 10 nΩ at 4.2 K, following the temperature dependence measured previously [17].

Micro-CT imaging revealed significant voids in an early prototype termination. The terminations reported here may have similar voids. These voids can block the current flow and increase the joint resistance. These voids can lead to the high joint resistance for Cable 1c that had the same configuration as the prototype termination. Voids, albeit smaller, were also observed in the electrical terminations of similar dimensions for CORC® wires [11]. Filling solder under vacuum pressure, as demonstrated in [38], needs to be developed for future STAR® cables.

On a positive note, indium solder filled the small gaps between the Cu strands and STAR® wire, likely under capillary force (figure 16). The good electrical contact can enhance current transfer from the current leads to STAR® wires and among the wires inside the termination.

We suspect that the non-uniform critical currents among the wires caused the pronounced ramp-rate dependence in Cable 6a (figure 20), based on the qualitative results from the circuit modeling (figure A2). The calculation showed that the voltage across some of the wires can decrease at a higher ramp rate (figure A3).

The calculation also showed that the ramp-rate dependence would disappear when all the wires had identical critical current, n value and termination resistance. Neither would the voltage across the wires decay at the current plateau. A strong ramp-rate dependence can therefore indicate that the electrical properties vary significantly among the STAR® wires in a 6-around-1 cable.

Contrary to the measured voltage, the solenoid field showed no obvious ramp-rate dependence (figure 21). This is because the transposed wires contributed equally to the center solenoid field per unit current in each wire. Even though each wire can carry different currents at different ramp rates, the solenoid field remained the same for the same total cable current.

7.3. Next steps

A thinner STAR® wire carrying a higher current will increase the whole-cable current density, J_e, essential for high-field accelerator magnets. Cable 6a had a relatively low J_e of 56 A mm^{-2} at 77 K, self-field. AMPeers recently reported a STAR® wire containing four REBCO tapes manufactured by the advanced MOCVD process [33]. The wire has a diameter of 1.51 mm and a critical current of 420 A at 77 K, self-field and 1070 A, 4.2 K and 30 T, both at a bend radius of 15 mm. Assuming an 80% retention in the critical current after cabling, as shown in both cable samples reported here, we expect a 6-around-1 cable using six such wires and a 1.628 mm diameter Cu core to have a J_e of 118 A mm^{-2} at 77 K, self-field, and 302 A mm^{-2} at 4.2 K, 30 T. A 6-around-1 cable can reach a J_e of 580 A mm^{-2} at 4.2 K, 30 T, if we retain the transport performance of the 1.51 mm diameter STAR® wire in a 1.1 mm diameter wire. Such a J_e meets or exceeds the conductor performance used in the design of magnets generating a dipole field of 20 T [1, 2].

The mechanical strength of the 6-around-1 cable should be measured, including the tensile strength and the strength against the

transverse compressive stress. An effective impregnation approach to support individual REBCO tapes in STAR® wires against the electromagnetic forces needs to be developed [33].

It is essential to make longer cable samples and to wind and test them in various magnet configurations. The test results will allow us to further improve the viability and performance of a 6-around-1 cable using STAR® wires for high-field magnet applications.

8. Conclusions

We made and tested two transposed 6-around-1 cable using high-temperature superconducting STAR® wires. The STAR® wires had a diameter of 1.8 — 1.9 mm, containing 7 — 9 REBCO tapes. One cable, Cable 1c, was 0.6 m long using a single STAR® wire. The other cable, Cable 6a, was 1.5 m long with a diameter of 5.7 mm. Both cables had a pitch length of 52 mm. We learned the following:

- We can make and test 6-around-1 cables using STAR® wires, including a method to install electrical terminations to the cable samples. Cable 6a reached 1448 A at 77 K, self-field but had a low n value of 4.5. The total joint resistance of both terminations in Cable 6a was 61 nΩ at 77 K, self-field.
- The cable samples retained about 80% of the total critical current of the STAR® wires before cabling, at a 20 μV criterion.
- The 20% loss in the critical current is puzzling and requires more studies comparing directly the critical current of STAR® wires before and after cabling.
- The cable samples can be bent to a radius of 30 mm with less than 5% reduction in the critical current at 77 K, self-field.
- At the same current above 1 kA, the voltage across Cable 6a increased with a higher ramp rates of the cable current. The performance remains to be measured for a cable with more uniform critical current and n values among its STAR® wires.
- The solenoid field generated by the coiled Cable 6a had no obvious ramp-rate dependence because each STAR® wire had the same contribution to the field per unit current in the wire, suggesting a benefit of a transposed cable configuration.

Our results demonstrated a first step toward a 6-around-1 cable using STAR® wires. The results set a stage for further development toward a high-current, flexible and transposed conductor for high-field magnet applications.

Acknowledgments

CF, EG, SRK, HN and HT fabricated and tested the STAR® wires. HCH made the 6-around-1 cable samples, developed the flute-type termination technique and the experimental setup for the measurements at LBNL. NC and GM performed the micro-CT scans. We thank Mark Krutulis of LBNL for helping with the cable fabrication.

We thank the following colleagues from the U.S. Magnet Development Program: Alexander Zlobin at Fermi National Accelerator Laboratory (FNAL) for raising the question if a 6-around-1 cable can be made from STAR® wires; Anis Ben Yahia and Ramesh Gupta from BNL, Vadim Kashikhin and Vito Lombardo from FNAL, for the discussions on the locations of voltage taps and their impact on the measurement and interpretation of $V(I)$ curves.

The work was supported by SBIR award DE-SC0021689 from the U.S. Department of Energy, Office of High-Energy Physics. The

work at LBNL was also supported by the U.S. Magnet Development Program through Director, Office of Science, Office of High Energy Physics of the US Department of Energy under Contract No. DEAC02-05CH11231.

We thank the reviewers for their comments and suggestions on the title, impact of conductor transposition on current distribution among the tapes, and the observed performance degradation after cabling and winding into multiple turns.

One author, VS, has financial interest in AMPeers.

Appendix A. Simulation of the cable behavior

We used two models to help interpret and understand the measurement data.

The first is a circuit model following the previous work [25, 36, 39–43]. Each STAR® wire was represented by a termination resistance, a nonlinear voltage source, and a self inductance. A resistance replaced the nonlinear voltage source for the central Cu wire. Figure A1 shows a schematic of the circuit model for Cable 6a.

We assumed a termination resistance of 3 nΩ at each end of the wires to match the measured 1 nΩ value of Cable 6a. The voltage source in Wire i, V_i, was given by $V_c(I_i/I_{c,i})^{n_i}$, where the I_c value for each wire was from table 1. The n value for each wire was set to 4.5 to match the measured n value of Cable 6a. The self and mutual inductance were calculated by approximating the strands as straight and parallel wires [44]. Table A1 lists the parameters used in the circuit model for Cable 6a. The self-field effect was neglected. Heat generation due to Joule heating or ac losses was not considered.

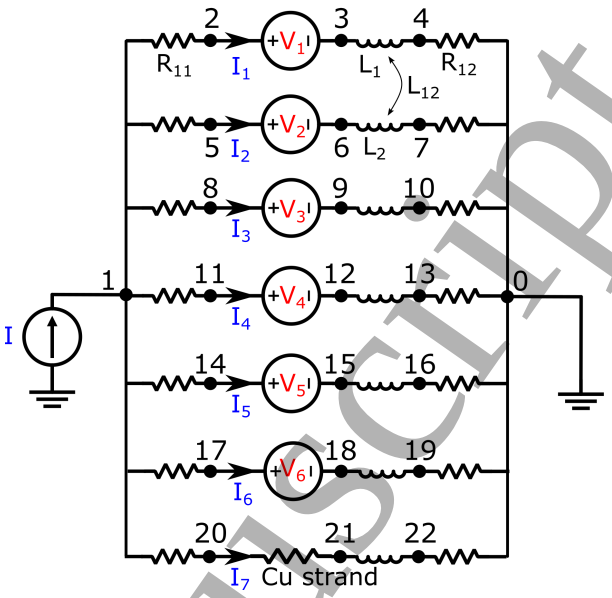

Figure A1. A circuit model for Cable 6a.

Table A1. Parameters for the circuit model. The first six wires are STAR® wires. The 7th wire is the central Cu strand. $L_{i,i}$ the self-inductance of the i-th wire. $L_{i,j}$ is the mutual inductance between the i-th and j-th wires.

Parameter	Value	Remarks
$R_{i,1}$, $R_{i,2}$	3 nΩ	$i = 1, \ldots, 7$
$I_{c,i}$	table 1	$i = 1, \ldots, 6$
n_i	4.5	$i = 1, \ldots, 6$
$L_{i,i}$	2.21 μH	$i = 1, \ldots, 7$
$L_{1,2}$	1.93 μH	Mutual inductance
$L_{1,4}$	1.76 μH	
$L_{1,6}$	1.72 μH	
R_{Cu}	1 mΩ	77 K value

We used NGSPICE [45] to calculate the current and voltage in the circuit model.

Figure A2 shows the calculated voltage across Wire 5, between Nodes 14 and 15 in figure A1, and the current in the wire, as a function of cable current and its ramp rate. At the same cable current, the voltage increased when the cable current ramped faster. When the current stopped ramping, the voltage and current decayed to those of

the dc case. The calculated voltage across the cable, between Nodes 1 and 0, also showed a similar behavior. Contrarily, the voltage across Wire 1 decreased with a higher ramp rate of the current (figure A3).

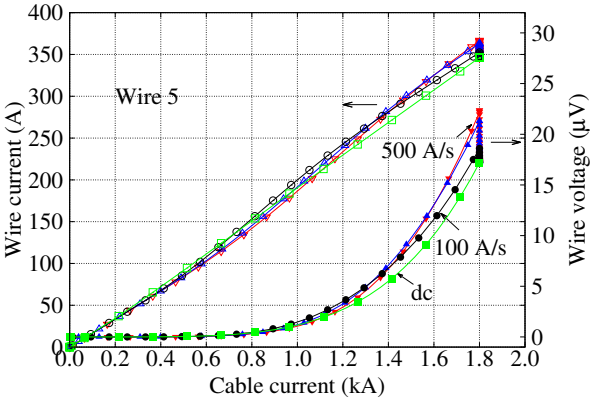

Figure A2. Calculated voltage across Wire 5 and the current in the wire as a function of cable current. Open symbols on the primary y axis: wire current. Solid symbols on the secondary y axis: wire voltage.

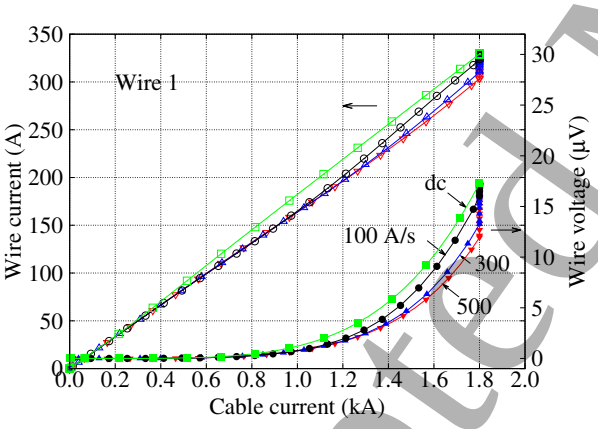

Figure A3. Calculated voltage across Wire 1 and the current in the wire as a function of cable current. Open symbols on the primary y axis: wire current. Solid symbols on the secondary y axis: wire voltage.

As the tapes are twisted but not transposed in a STAR® wire and the critical current of individual tapes scales with the tape width, the current distribution among the tapes can be non-uniform at dc condition and when current ramps [41]. Further measurements are required to clarify the impact of non-uniform current distribution in the STAR® wires on the cable performance at a high current ramp rate.

The second model calculated the magnetic fields generated by the cable. We considered two cases: the straight cable and the multi-turn bending for both cable samples. Each STAR® wire was modeled using a Biot-Savart conductor in Opera [46]. Figure A4 shows the model for the 6.5-turn solenoid wound by Cable 6a.

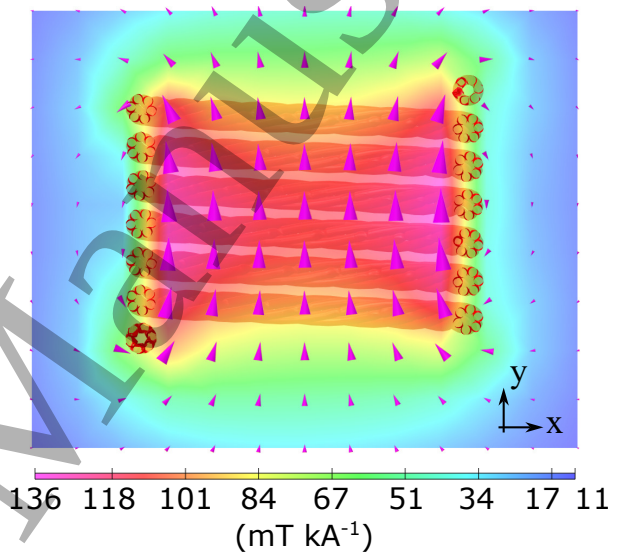

Figure A4. The vectors of the flux density on the $z = 0$ cut plane of the model for the 6.5-turn solenoid wound by Cable 6a. The colormap shows the flux density per kA total current in the cable on the $z = 0$ cut plane.

Table A2 lists the calculated flux density transverse to the wire axis for different cases, together with the solenoid component at the coil center.

References

[1] Ferracin P, Ambrosio G, Arbelaez D, Brouwer L, Barzi E, Cooley L, Garcia Fajardo L, Gupta R, Juchno M, Kashikhin V, Marinozzi V, Novitski I, Rochepault E,

Table A2. Calculated flux density per kA total current in both cables and the solenoid component at the coil center.

Case	Value (mT)
B_{trans}, 1c, straight	6.3
B_{trans}, 1c, 1.5-turn	65
B_{trans}, 6a, straight	40
B_{trans}, 6a, 6.5-turn	117
B_{y} at solenoid center	113

Stern J, Zlobin A and Zucchi N 2022 *IEEE Trans. Appl. Supercond.* **32** 4000906 ISSN 1051-8223, 1558-2515

[2] Ferracin P, Ambrosio G, Anerella M, Arbelaez D, Brouwer L, Barzi E, Cooley L D, Cozzolino J, Garcia Fajardo L, Gupta R, Juchno M, Kashikhin V V, Kurian F, Marinozzi V, Novitski I, Rochepault E, Stern J, Vallone G, Yahia B and Zlobin A V 2023 *IEEE Trans. Appl. Supercond.* **33** 4002007 ISSN 1051-8223, 1558-2515

[3] Prestemon S, Amm K, Cooley L, Gourlay S, Larbalestier D, Velev G and Zlobin A 2020 The 2020 updated roadmaps for the US Magnet Development Program http://arxiv.org/abs/2011.09539

[4] Shen T, Garcia Fajardo L, Myers C, Hafalia A, Rudeiros Fernández J L, Arbelaez D, Brouwer L, Caspi S, Ferracin P, Gourlay S, Marchevsky M, Pong I, Prestemon S, Teyber R, Turqueti M, Wang X, Jiang J, Bosque E, Lu J, Davis D, Trociewitz U, Hellstrom E and Larbalestier D 2022 *Physical Review Accelerators and Beams* **25** 122401

[5] Garcia Fajardo L, Shen T, Wang X, Myers C, Arbelaez D, Bosque E, Brouwer L, Caspi S, English L, Gourlay S, Hafalia A, Martchevskii M, Pong I and Prestemon S 2021 *Superconductor Science and Technology* **34** 024001 ISSN 0953-2048

[6] Shen T and Garcia Fajardo L 2020 *Instruments* **4** 17

[7] Gupta R, Amm K, Anerella M, Cozzolino J, Joshi P, Joshi S, Plate S, Sampson W and Wanderer P 2020 *IEEE Trans. Appl. Supercond.* **30** 4000106 ISSN 1558-2515

[8] Kashikhin V, Lombardo V and Velev G 2019 Magnet design optimization for future hadron colliders (JACOW Publishing, Geneva, Switzerland) pp 4307–4310 ISBN 9783954502080 https://doi.org/10.18429/JACoW-IPAC2019-THPTS084

[9] Kashikhin V V, Cohan S, Lombardo V, Turrioni D, Mai N, Chavda A K, Sarangi U, Korupolu S, Peram J, Anil A, Goel C, Sandra J S, Yerraguravagari V, Schmidt R, Selvamanickam V, Majkic G, Galstyan E and Selvamanickam K 2023 (*Preprint* 2307.12954)

[10] Wang X, Dietderich D R, DiMarco J, Ghiorso W B, Gourlay S A, Higley H C, Lin A, Prestemon S O, van der Laan D and Weiss J D 2019 *Superconductor Science and Technology* **32** 075002

[11] Wang X, Abraimov D, Arbelaez D, Bogdanof T J, Brouwer L, Caspi S, Dietderich D R, DiMarco J, Francis A, Garcia Fajardo L, Ghiorso W B, Gourlay S A, Higley H C, Marchevsky M, Maruszewski M A, Myers C S, Prestemon S O, Shen T, Taylor J, Teyber R, Turqueti M, van der Laan D and Weiss J D 2020 *Superconductor Science and Technology* **34** 015012 ISSN 0953-2048

[12] van der Laan D C 2009 *Superconductor Science and Technology* **22** 065013

[13] Weiss J D, Mulder T, ten Kate H J and van der Laan D C 2017 *Superconductor*

Science and Technology **30** 014002 and references therein.

[14] Luo W, Kar S, Xu A, Li X, Yahia A B and Selvamanickam V 2017 *IEEE Trans. Appl. Supercond.* **27** 6602705 ISSN 1051-8223

[15] Kar S, Luo W, Sai Sandra J, Majkic G and Selvamanickam V 2019 *IEEE Trans. Appl. Supercond.* **29** 6602605

[16] Uglietti D, Kang R, Wesche R and Grilli F 2020 *Cryogenics* **110** 103118 ISSN 0011-2275

[17] Wang X, Bogdanof T J, Ferracin P, Ghiorso W B, Gourlay S A, Higley H C, Kadiyala J K, Kar S, Lee R, Luo L, Maruszewski M A, Memmo R, Myers C S, Prestemon S O, Sandra J S, Selvamanickam V, Teyber R, Turqueti M and Wu Y 2022 *Superconductor Science and Technology* **35** 125011 ISSN 0953-2048

[18] Wilson M N 1983 *Superconducting magnets* (New York: Oxford University Press) chap 12

[19] Uglietti D 2019 *Superconductor Science and Technology* **32** 053001 ISSN 0953-2048 and references therein

[20] Fleiter J 2021 Rutherford cables for HL-LHC superconducting magnets https://indico.cern.ch/event/1077978/

[21] Schlachter S I, Goldacker W, Grilli F, Heller R and Kudymow A 2011 *IEEE Transactions on Applied Superconductivity* **21** 3021–3024 ISSN 1558-2515

[22] Kario A, Vojenciak M, Grilli F, Kling A, Ringsdorf B, Walschburger U, Schlachter S I and Goldacker W 2013 *Superconductor Science and Technology* **26** 085019 ISSN 0953-2048

[23] Uglietti D, Bykovsky N, Sedlak K, Stepanov B, Wesche R and Bruzzone P 2015 *Superconductor Science and Technology* **28** 124005

[24] Takayasu M 2021 *Superconductor Science and Technology* **34** 125020 ISSN 0953-2048

[25] Knoopers H G, ten Kate H H J and van de Klundert L J M 1985 Distribution of currents in a 6-strand superconducting cable *Proceedings of the 9th International Conference on Magnet Technology* pp 539–542

[26] Liang Y, Wu W, Mei E, You W, Lu J, Ou X, Yao Q and Ma L 2022 *IEEE Transactions on Applied Superconductivity* **32** 4001905 ISSN 1558-2515

[27] Wang D, Xi D, Wang Q, Feng J, Pan X, Chen C, Yan G, Zhang P and Li J 2020 *IEEE Transactions on Applied Superconductivity* **30** 6200205 ISSN 1558-2515

[28] Diaczenko N, Elliott T, Liang G, McIntyre P M, Motowidlo L R, Soika R and Yavuz M 2000 *Physica. C, Superconductivity* **341-348** 2551–2554 ISSN 0921-4534

[29] Shen T, Li P, Jiang J, Cooley L, Tompkins J, McRae D and Walsh R 2015 *Superconductor Science and Technology* **28** 065002 ISSN 0953-2048

[30] Mulder T, Dudarev A, Mentink M, Dhallé M and ten Kate H 2016 *IEEE Transactions on Applied Superconductivity* **26** 4801704 ISSN 1558-2515

[31] Mulder T, Dudarev A, van der Laan D C, Mentink M G T, Dhallé M and ten Kate H H J 2015 Optimized and practical electrical joints for CORC type HTS cables *Materials Science and Engineering Conference Series* (*Materials Science and*

Engineering Conference Series vol 102) p 012026

[32] Iwasa Y 2009 *Case studies in superconducting magnets: design and operational issues* (Springer) chap 6, p 370 2nd ed

[33] Galstyan E, Kadiyala J, Paidpilli M, Goel C, Sandra J S, Yerraguravagari V, Majkic G, Jain R, Chen S, Li Y, Schmidt R, Jaroszynski J, Bradford G, Abraimov D, Chaud X, Song J and Selvamanickam V 2023 *Superconductor Science and Technology* **36** 055007 ISSN 0953-2048

[34] Kar S, Sandra J S, Luo W, Kochat M, Jaroszynski J, Abraimov D, Majkic G and Selvamanickam V 2019 *Superconductor Science and Technology* **32** 10LT01 ISSN 0953-2048

[35] Paidpilli M and Selvamanickam V 2022 *Superconductor Science and Technology* **35** 043001 ISSN 0953-2048

[36] Willering G P, van der Laan D C, Weijers H W, Noyes P D, Miller G E and Viouchkov Y 2015 *Superconductor Science and Technology* **28** 035001

[37] Takayasu M, Chiesa L, Bromberg L and Minervini J V 2012 *Superconductor Science and Technology* **25** 014011

[38] Hartwig Z S, Vieira R F, Sorbom B N, Badcock R A, Bajko M, Beck W K, Castaldo B, Craighill C L, Davies M, Estrada J, Fry V, Golfinopoulos T, Hubbard A E, Irby J H, Kuznetsov S, Lammi C J, Michael P C, Mouratidis T, Murray R A, Pfeiffer A T, Pierson S Z, Radovinsky A, Rowell M D, Salazar E E, Segal M, Stahle P W, Takayasu M, Toland T L and Zhou L 2020 *Superconductor Science and Technology* **33** 11LT01 ISSN 0953-2048

[39] Pothavajhala V, Graber L, Kim C H and Pamidi S 2014 *IEEE Trans. Appl. Supercond.* **24** 4800505 ISSN 1051-8223

[40] Zermeno V, Krüger P, Takayasu M and Grilli F 2014 *Superconductor Science and Technology* **27** 124013 ISSN 0953-2048

[41] Michael P C, Bromberg L, van der Laan D C, Noyes P and Weijers H W 2016 *Superconductor Science and Technology* **29** 045003 ISSN 0953-2048

[42] Araujo Martínez A C, Ji Q, Prestemon S O, Wang X and Maury Cuna G H I 2020 *IEEE Trans. Appl. Supercond.* **30** 6600605 ISSN 1558-2515

[43] Teyber R, Weiss J, Marchevsky M, Prestemon S and van der Laan D 2022 *Scientific reports* **12** 22503 ISSN 2045-2322

[44] Grover F W 2004 *Inductance calculations* (Dover Publications, Inc.) chap 5, pp 31–35

[45] ngspice https://ngspice.sourceforge.io/index.html

[46] Dassault Systèmes Opera electromagnetics finite element software suite http://operafea.com/